nature communications

Article

https://doi.org/10.1038/s41467-025-62049-6

Sustainable Bi-directional thermoregulation fabric for clothing microclimate

Received: 11 May 2024

Accepted: 4 July 2025

Published online: 22 July 2025

Check for updates

Yanyan Lin[1,2], Chengran Qu[1], Xueqin Li[1], Chengfeng Ding[1], Xianfeng Wang[1,2] ✉, Jianyong Yu[2] & Bin Ding[2] ✉

Maintaining the balance of clothing microclimate is critical for human health management. An ideal smart textile should possess key characteristics such as active thermoregulation, moisture permeability, and stable working performance. However, such a fabric that encompasses all these capabilities is rarely reported. Herein, we report a sustainable and durable bi-directional thermoregulation fabric (Bi-DTF) by hierarchical structural engineering strategy. This advancement stems from the programmability of the molecular chains, aiming to reduce chain aggregation, improve functional particle compatibility, and build dynamic stress-dissipative networks, thus fully enhancing the robustness of composite fibrous membranes. The optimized Bi-DTF substantially eliminates the heat/cold irritation caused by environmental switching, featuring high energy storage density ($4.1\,\mathrm{kJ\,m^{-2}}$) and stable work performance even after 50 standard washing cycles and 500 rubbing cycles. Compared with commercial textiles, Bi-DTF offers a maximum thermal temperature difference of only 2.3 °C and a cooling temperature difference of 2.6 °C when going through the heating and cooling cycles. Due to its exceptional personal thermoregulation performance and long-term stability, this proposed strategy exhibits considerable potential for the application of healthcare, outdoor sports, and protective clothing.

Clothing, as an indispensable barrier between the skin and the environment, is critical in regulating the wearing comfort of the human body in daily life[1]. By exchanging heat and moisture with the outside environment through the medium of textiles, the body-textile microclimate is formed between the clothing and the human skin[2,3]. A body-textile microclimate with appropriate temperature and humidity (32 ± 1 °C, $50 \pm 10\%$ RH) provides both physical and psychological comfort for the individual, however, its equilibrium is often disrupted due to weather or human behaviors[4,5]. For example, when going from a comfortable environment to a hot or cool environment, the human body is unable to quickly adapt to the transition, resulting in unpleasant heat/cold irritation and possibly even medical emergencies[6]. With the ongoing development of the national health system, people are gradually shifting from a negative lifestyle based on overdraft and medical treatment to a healthy lifestyle centered on healthcare and prevention. Therefore, wearable thermoregulatory clothing that can keep the body-textile microclimate in a comfortable range has been a long-sought but challenging aim for smart textiles[7,8].

Active responsive textiles allow for the warming or cooling of the human body depending on the surroundings[9,10]. By sensing the stimuli (e.g., temperature, humidity, light, electricity, and mechanical), clothing is able to adjust the exchange efficiency with the external environments or realize energy absorption/release[11–14]. Recently, phase change materials used to regulate temperature fluctuations without additional energy have attracted widespread interest from researchers[15–17]. Fiber-based phase change textiles are mainly prepared by post-finishing, capsulation embedding, or skin-core fiber structure[18]. Liu et al. proposed to impregnate paraffin into nonwoven,

---

[1]State Key Laboratory of Advanced Fiber Materials, College of Textiles, Donghua University, Shanghai 201620, China. [2]Innovation Center for Textile Science and Technology, Donghua University, Shanghai 200051, China. ✉e-mail: wxf@dhu.edu.cn; binding@dhu.edu.cn

but this suffered from leakage defect[19]. In recent years, electrospinning technology has been widely used to prepare phase change textiles for personal thermal management due to its high structural designability[20]. Li et al prepared multifunctional films with sufficient enthalpy and the phase change capsules were strung on the fibers with a "candied haws stick" structure[21]. However, electrospinning fibrous membranes have been plagued by low strength and poor durability for a long time. This makes it difficult for the prepared fibrous membranes to meet the requirements of daily use. Polyurethane (PU) elastomers have attracted much attention due to their excellent mechanical properties and applicability[22]. Structural design strategies based on various intermolecular interactions (e.g., hydrogen bonding, π-π stacking, and ionic cross-linking) have been widely explored, indicating the feasibility of electrospinning fibrous membranes with high strength and elasticity[23]. It is worth noting that the strong entanglement of polymer networks makes it difficult to develop electrospun fibrous membranes with ordered molecular chains and satisfactory mechanical properties[24]. In addition, it remains another challenge to improve the particle loading and homogeneity of membranes to ensure their reliability in functional applications.

Herein, we conceive a hierarchical structural engineering strategy by combining the hydrogen-bonding interaction network and physical bonding sites to fabricate the toughness composite fibrous membrane with efficient resistance to external forces. The PU polymer with high hydrogen-bonding content was constructed and through molecular dynamics (MD) simulations, we found that aggregation of molecular chains can be reduced by adding ethanol (EtOH), which leads to easier molecular movement and orientation. In particular, we combine this strategy with the electrospinning technique to shape functional nanoparticles into PU matrix. The nanoparticles were distributed in the interconnected fibers and showed their high binding stability. Moreover, the bi-directional thermoregulation fabric (Bi-DTF) was assembled, which could eliminate the irritation from environmental switching, extending the body's comfort. The as-prepared Bi-DTF exhibits high strength (12.7 MPa) with superior elastic recovery, continuous workability, as well as excellent durability (500 rubbing or 50 washing cycles).

Results

Design and processing of Bi-DTF

We designed the Bi-DTF according to three crucial considerations: (i) the fiber substrate must be strong enough; (ii) the functional particles must be well-assembled into the fibers; and (iii) the work performance must be stable during the long-term service life. The first requirement was enabled by employing hydrogen-bonded assisted engineering in PU polymers. As depicted in Fig. 1a, the multiple hydrogen-bonding interactions facilitate effective energy dissipation under external forces. The fabrication of the PU fibrous membrane began with the preparation of a precursor solution containing polymer and solvents. Notably, the N, N-dimethylformamide (DMF) was a benign solvent, while the addition of EtOH effectively minimized the intermolecular chain entanglement. The MD simulations were conducted to demonstrate the states of PU, PU/DMF, and PU/DMF/EtOH systems. As revealed in Fig. 1b, c and Supplementary Fig. 1, the chain in the PU/DMF/EtOH system exhibited a more loose stacking state due to the larger free volume[25]. Besides, the contribution of van der Waals and electrostatic forces to the overall cohesion energy in different systems was further compared (Fig. 1d). The results proved that the contribution of van der Waals force in the PU system was as high as 86.8%, which is the main cause for the entanglement of polymer chains[26]. After the addition of DMF, the contribution of van der Waals force decreased, and that of electrostatic force increased, which indicates that the original equilibrium of PU gradually disintegrated. Obviously, EtOH further facilitated this phenomenon, making it easier for the molecular chains of the PU to be reordered and arranged by external forces.

Subsequently, the functional nanoparticles were incorporated into the PU solution, the softened PU molecular chains were more conducive to the dispersion of particles (Fig. 1e). Under the stretching effect of the high-voltage electrostatic field, the PU molecular chains were oriented along the fiber axis and encapsulated the nanoparticles. Through the adjustment of the curing rate, the dual cross-linked composite PU fibers with high nanoparticle loading were successfully prepared. Typically, phase change nanocapsules (PCN) and boron nitride nanosheets (BN) were added to the PU to develop phase change membrane (PC-M, Fig. 1f) and thermal conductive membrane (TC-M, Fig. 1g), respectively. As seen from the inset images, the nanoparticles were uniformly distributed in the fibers, which helps to prevent the shedding of functional components. Through dual-crosslinked structural design, the Janus fibrous membrane named Bi-DTF was fabricated, and the thickness of fabric was controlled at PC-M: TC-M = 2:1 (Fig. 1h and Supplementary Fig. 2). As shown in Fig. 1i, the Bi-DTF (~0.18 g) could successfully lift a 2 kg weight, equivalent to ~1100 times its mass, demonstrating its superior robustness. The Bi-DTF could attenuate stimuli caused by sudden fluctuations in ambient temperature through its well-integrated thermal characteristics, thereby establishing a relatively stable and comfortable body-textile microenvironment for individuals (Supplementary Fig. 3). This property was substantiated through empirical experiments in which volunteers wore T-shirts embedded with various fabric samples (Supplementary Figs. 4, 5). Compared to commercial textiles, the Bi-DTF exhibited lower temperatures when experiencing hot environments (Fig. 1j), and higher temperatures in colder environments (Fig. 1k), attributed to its fast thermal response and efficient energy storage/release mechanisms. Especially in summer, conventional textiles may trigger thermal discomfort during temperature variations, however, Bi-DTF addresses this issue.

Synthesis and thermal properties of fibrous membranes

Polyester polyols (HDPOL) were employed as soft segments, isophorone diisocyanate (IPDI) and N, N-bis(2-hydroxyethyl)oxamide (BHO) were used as hard segments, and chain extender to prepare PU elastomers by the solvent-free polymerization. The synthetic route and characterization of the PU are shown in Supplementary Figs. 6–9 and Table 1. The abundant carbamate and amide bonds could provide a large number of hydrogen bond donors and acceptors to incorporate high-density and strong interactions in the microdomains[27]. The hydrogen bonding of the PU was investigated by FTIR. As shown in Fig. 2a, the signal in the wavenumber range of 1600 − 1800 cm^{-1} could be attributed to the C = O group[28]. Further analysis of this region through peak fitting revealed that the as-prepared PU elastomer was deconvolved into four sub-peaks (Supplementary Table 2). These sub-peaks can be assigned as follows: the free carbonyl groups ≈1731 cm^{-1}, the hydrogen-bonded disordered carbonyl groups ≈1663 cm^{-1}, and the hydrogen-bonded ordered carbonyls groups from 1706 to 1629 cm^{-1}, respectively. The bonded content in PU elastomers was determined to be as high as 78.1%. The packing state of the structure in PU was further performed. As depicted in Fig. 2b, the aggregation of the hard segments of the polymer occurs due to hydrogen bonding cross-linking, leading to the formation of a phase-separated structure between the hard and soft domains. The calculated cohesive energy density (CED) of the system was 367.4 J cm^{-3}, which was usually lower than 300 for elastomer[29,30]. In addition, the distribution of chain segments in the theoretical simulation showed that the hard segments in the PU system were more dispersed in the soft segments, which is conducive to the elimination of the stress concentration and the enhancement of the energy dissipation efficiency[31]. The microphase separation structure was further evidenced by small angle X-ray scattering (SAXs) (Fig. 2c). The average distance between hard phases was determined to be 10.8 nm, indicating a smaller average distance between the hard domains and higher hydrogen bonding density. In contrast, excessive

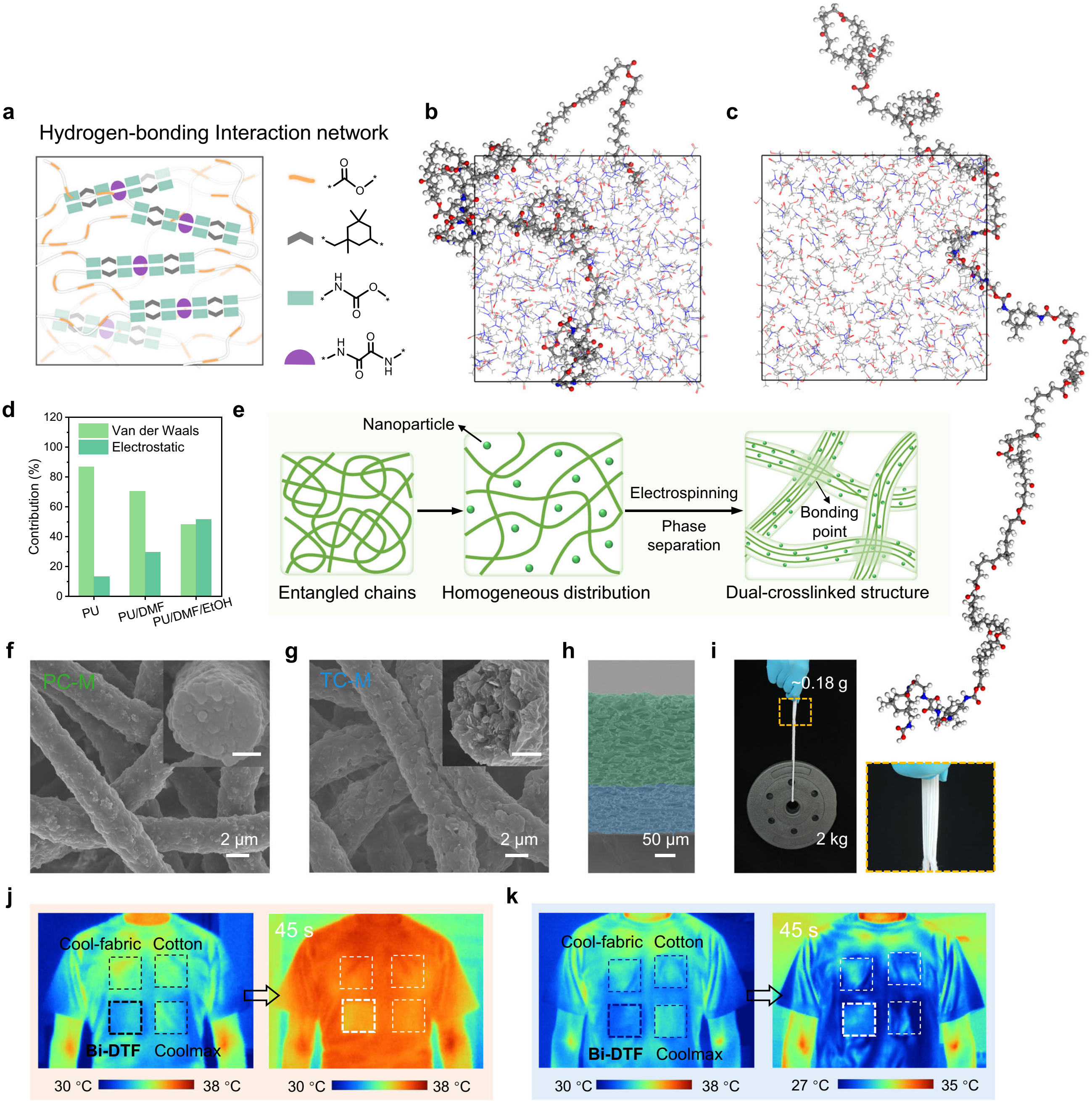

Fig. 1 | **Structural architecture and principle of the Bi-DTF. a** The hydrogen-bonding interaction network in PU. The MD simulations of (**b**) PU/DMF and (**c**) PU/DMF/EtOH systems. **d** Comparison of contribution about intermolecular forces to cohesion energy. **e** Schematic diagram of dual cross-linked composite fibrous membrane. The SEM images of (**f**) PC-M and (**g**) TC-M. The insets picture the cross-sectional morphology of fiber, with scale bars of 1 μm. **h** The cross-sectional SEM image of Bi-DTF. **i** Digital photographs showing that the Bi-DTF can lift a weight of 2 kg. Infrared images of a volunteer wearing the composite T-shirt experiencing the (**j**) hot and (**k**) cold environments, respectively.

hard domain aggregation may impair the compatibility between soft and hard segments, resulting in stress concentration. Consequently, the precise modulation of phase-separated morphology, coupled with the establishment of dense hydrogen bonding networks within the PU, plays a pivotal role in optimizing the material's mechanical performance.

The synthesis of composite functional fibers with dual-crosslinked networks depends on the molecular chain movement, nanoparticle dispersion, and phase separation with the charged jets. Based on the aforementioned analysis, EtOH was introduced during the preparation of the precursor solution, and the formation mechanism of the composite structure is summarized in Fig. 2d. The purpose of the electrospinning is to generate a continuous jet from the metal needle tip. Initially, PU dominates the blend solution, nanoparticles are dispersed in the polymer solution and confined into PU fibers. EtOH promotes the mobility of the polymer chains and reduces the aggregation of chains, resulting in a decrease in surface tension (Step I). Here, PU fibers act as the confining template for the particles. Compared to microspheres, the confinement of nanoparticles into polymer fibers to obtain one-dimensional colloidal chains is a relatively simple process due to their size feature[32]. It can be observed from step II that during the jet thinning process, the molding of the composite fibers is controlled by the viscosity of the blend solutions. The PU works as a binder to produce an adhesive force between particles; and this force

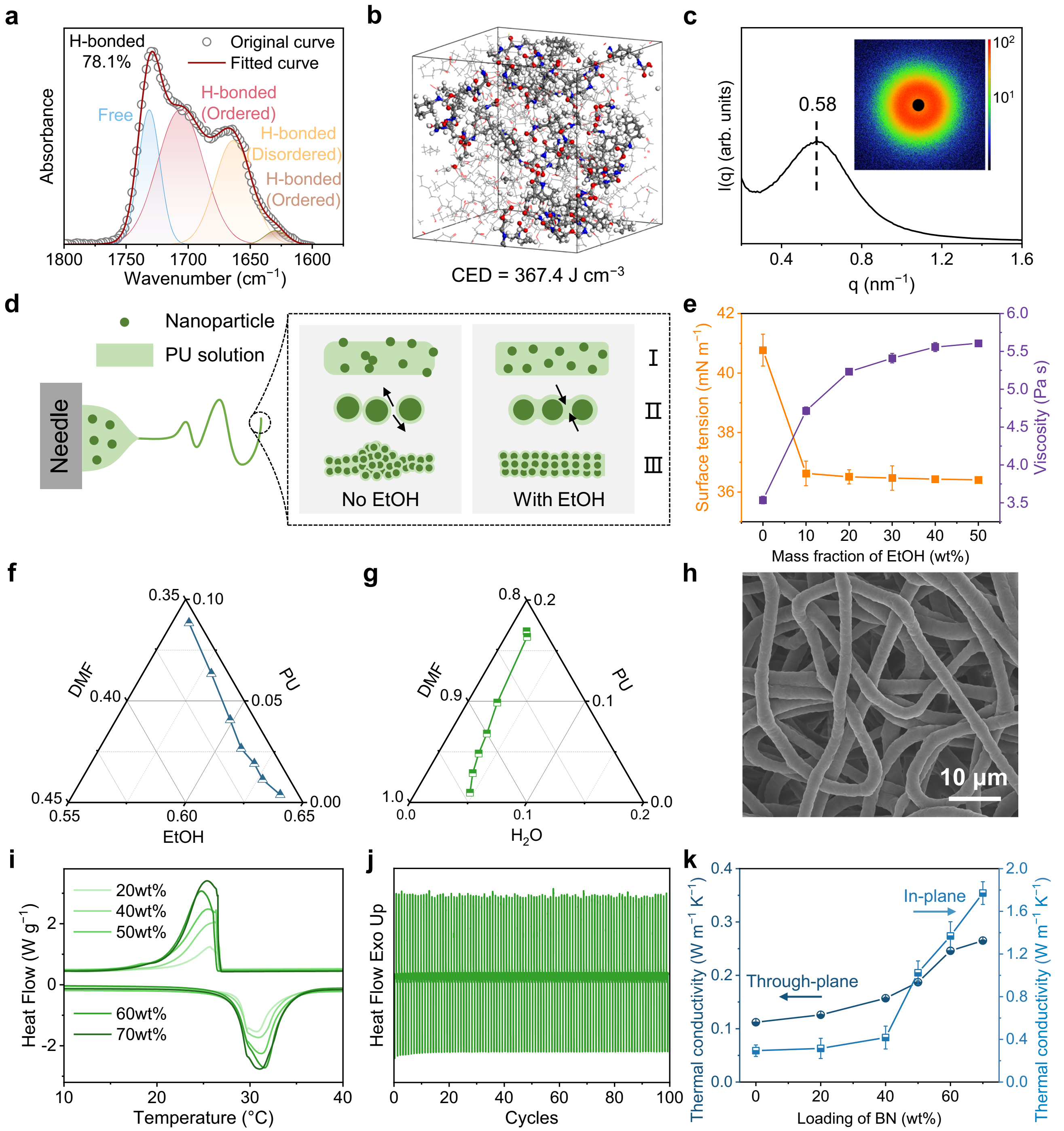

Fig. 2 | Construction and characterization of Bi-DTF. a FTIR spectra of the PU elastomer in the C = O stretching vibration region. **b** Snapshot of the all-atom MD simulation of PU structure. **c** 1D SAXS pattern of the PU elastomer. Inset: 2D SAXS pattern. **d** Schematic representation of the formation mechanism of composite fibers under different steps. **e** Solution properties under different mass fractions of EtOH. Ternary phase diagrams of the (**f**) PU/DMF/EtOH and (**g**) PU/DMF/H_2O systems. **h** The SEM image of PU fibrous membrane. **i** DSC curves of PC-M with various PCN loading. **j** Cyclability test of PC-M. **k** Thermal conductivity changes about TC-M with BN content varying. The error bars for (**e** and **k**) represent mean ± SD ($n = 5$ independent samples).

is proportional to the viscosity[33]. Thus, uniform colloidal fibers are obtained when the adhesive force between the particles is stronger. The above hypothesis can be substantiated by evaluating the properties of solutions. With the addition of EtOH in solvents, a sharp decrease in surface tension was noted, while the viscosity of the solution progressively increased (Fig. 2e).

With the continuous drafting of the electrostatic force, the solvent diffuses with the non-solvent and exchanges at the interface between the spinning jets and the water vapor, the wrapped particles are packed and assembled into the fibers, leading to the formation of the composite fibers (Step III, Fig. 2d)[34]. We experimentally analyzed the phase separation behavior of the precursor solution. In the ternary phase diagram of PU/DMF/EtOH, the binodal curve is away from the PU-DMF axis, which suggests that a high proportion of EtOH still leaves the solution in a homogeneous liquid phase (Fig. 2f, Supplement Fig. 10a). In the ternary phase diagram of PU/DMF/H_2O, the binodal curve is closer to the PU-DMF axis, implying that as long as a small amount of water is needed, the phase separation of PU solution can be induced (Fig. 2g, Supplement Fig. 10b). Through the adjustment of the curing rate, the dual cross-linked PU fibrous membrane with both physically bonded structure and hydrogen bonding network was successfully prepared, as shown in Fig. 2h, Supplementary Fig. 11 and Table 2. Furthermore, It can be found that it is difficult to form uniform fibers in the absence of EtOH (Supplementary Fig. 12). Therefore, tunable structures of PU/nanoparticles could be obtained by adjusting the weight ratio of EtOH, two components, and water.

The morphological changes in the PC-M with different doping ratios are displayed in Supplementary Fig. 13, where PCN was regularly enriched in the fibers with the increase of loading. The thermal energy storage property of PC-M was studied by differential scanning calorimeter (DSC). As shown in Fig. 2i, the absorption and exothermic peaks were narrow and concentrated, with increasing PCN content, the peak height gradually increased. Specifically, the crystallization and melting temperatures of PC-M with 60 wt% PCN loading are 24.8 and 31.7 °C, and the corresponding enthalpies are 66.3 and 64.2 J g^{-1}, respectively, which is slightly lower than theoretical enthalpies, revealing the effective loading of PCN in nanofibers (Supplementary Fig. 14 and Table 3). Furthermore, the heat absorption/exothermic abilities of the fibers remained stable even after 100 heating and cooling cycles (Fig. 2j, Supplementary Fig. 15 and Table 4), which indicates the thermal stability of the prepared membranes. Conventional textiles lacked timely interaction with temperature variations of the surroundings due to their low thermal conductivity[35]. In order to raise the thermal sensitivity of the fibrous membrane, The PU matrix is dopped with BN nanosheets, and the microstructures of TC-M with various loading are shown in Supplementary Fig. 16, where the interconnected BN builds up heat transfer pathways (Supplementary Fig. 17)[36]. The variation of thermal conductivities is shown in Fig. 2k and Supplementary Table 5, in which the through-plane and in-plane thermal conductivities of TC-M with BN loading of 50 wt% are 0.187 and 1.024 W m^{-1} K^{-1}, respectively. The good thermal conductivity provides a substantial foundation for the subsequent sensing of external temperature changes.

By comprehensively comparing and integrating the unique properties, the Bi-DTF with Janus structure was fabricated, as depicted in Supplementary Fig. 18–20 and Table 6-7. The Bi-DTF is light and thin (~90 g m^{-2}), with through-plane thermal conductivity of 0.163 W m^{-1} K^{-1} and melting enthalpy of 45.9 J g^{-1}, while the energy storage density is up to 4.1 kJ m^{-2}. Furthermore, the high-temperature thermal stability was experimentally verified. As shown in Supplementary Fig. 21, the octadecane (OD) melted and deformed rapidly at 80 °C, while the PCF maintained good shape stability due to its stable multiple encapsulation structure.

Mechanical and durability properties of Bi-DTF

Phase change fabrics developed in the previous studies showed poor mechanical properties due to size or dimensional incompatibility, making it difficult to meet consumer demand for long-lasting service performance (Supplementary Tables 8 and 9). Remarkably, the mechanical property of Bi-DTF was significantly improved by introducing the hierarchical cross-linked architecture. As shown in Fig. 3a, the tensile strength of PU elastomer was measured to be 60.4 MPa and elongation of 2309.4% at break, which showed an advantage with a toughness of up to 648.1 MJ m^{-3} that surpasses most reported materials (Supplementary Table 11). Moreover, cyclic stretching with increased strain and the recovery ability of elastomers was evaluated. The hysteresis loop gradually increased with strain improvement (Fig. 3b), which may be attributed to the gradient energy dissipation formed by the gradual breakage of the weak hydrogen bonds and strongly ordered hydrogen-bonded domains[37]. Besides, the cyclic tensile curve demonstrates that the mechanical properties of the material gradually recover and the broken hydrogen bonds are re-associated (Fig. 3c). This is due to the fact that the incorporation of BHO moieties provided abundant hydrogen-bonding sites, which acted as sacrificial bonds to dissipate energy through breaking and recombination (Fig. 3d)[38]. Collectively, the PU elastomers exhibit excellent tensile and elastic recovery abilities rendering it as the polymeric substrate with exceptional comprehensive mechanical properties.

Supplementary Fig. 22 presents the mechanical properties of electrospinning PU fibrous membranes with a mechanical strength of 32.5 MPa and elongation of 571.5% at break. With the increase of nanoparticles, the strength and elongation declined (Supplementary Fig. 23). Intriguingly, the Bi-DTF boasted a high breaking elongation of 243.9% and a tensile strength of 12.7 MPa (Fig. 3e), with a toughness of 18.3 MJ m^{-3}. The cyclic loading-unloading tensile curves of Bi-DTF at 50% strain are displayed in Fig. 3f. There was an obvious hysteresis in the first-cycle curve due to the force-induced hydrogen bond breaking leading to substantial energy dissipation. The 11th cycle occurred after 3 h, which is close to the cyclic loading-unloading curve of the first lap, suggesting good elastic recovery of the Bi-DTF. Fig. 3g further demonstrates that the prepared samples exhibit ultra-high elastic recovery capacity, which can significantly improve the fatigue resistance and reliability of the textiles during repeated deformation processes. To characterize the physical bonding properties of the Janus membrane, a peeling test was conducted with an overlap length of 4 cm and a width of 2 cm. As illustrated in Fig. 3h, the peel strength was 0.2 N cm^{-1}, and the slip displacement was ~ 8 cm, attributed to the good physical bonding between the fibers. The fracture energy of the Bi-DTF composites exhibited a remarkably high value (~20 J m^{-2}) in comparison to previously reported works[39], which typically range from 1 ~ 5 J m^{-2}. The mechanical performance of Bi-DTF can be attributed to the following factors: i) the multiple hydrogen bonds in the PU matrix, which allow dynamic molecular chains to break and reorganize; ii) the good compatibility of the particles with the polymeric substrate reducing stress defects; and iii) the physical binding points between fibers preventing inter-fiber slip. These factors significantly improved the energy dissipation efficiency upon external force.

Durability is the major issue impeding the practical applicability of the electrospinning membranes. Therefore, the abrasion resistance tests were performed on the Bi-DTF from different sides (Supplementary Fig. 24). It took 2000 standard friction cycles for the fracture of Bi-DTF (Supplementary Fig. 25). At 500 friction cycles, the mass retention of fibrous membranes was still as high as 95% (Fig. 3i). Due to the layer-by-layer deposition characteristic of electrospinning and the unique hierarchical crosslinked structure, the weight loss process of the fibrous membrane was manifested as the failure of physical points, fiber breakage, and layer-by-layer detachment of the fibrous membrane, which can effectively prevent the shedding of nanoparticles (Supplementary Fig. 26)[40]. In addition, Bi-DTF showed excellent detergent resistance, maintaining stable work performance even after 50 standard washes with less than 1% weight loss and plastic deformation (Fig. 3j, Supplementary Fig. 27 and Table 10). Additionally, the dyes were introduced to customize the textiles in different colors. The results showed that the films exhibited good optical properties, with chromatic aberration $DE^*_{ab} < 3$ over 50 washing cycles (Fig. 3k and Supplementary Fig. 28).

Evaluation of dynamic comfort performance

Although phase change textiles contribute thermal regulation capability, their low moisture permeability might result in a negative impact on the overall performance of the garment[41]. However, the previous studies tended to raise the enthalpies while disregarding the complicated heat-moisture interactions in the body-textile microclimate[42]. This contradiction failed to be adequately balanced for consideration in practical product design and it lacks substantial empirical backing. Therefore, in this study, Janus wettability was also

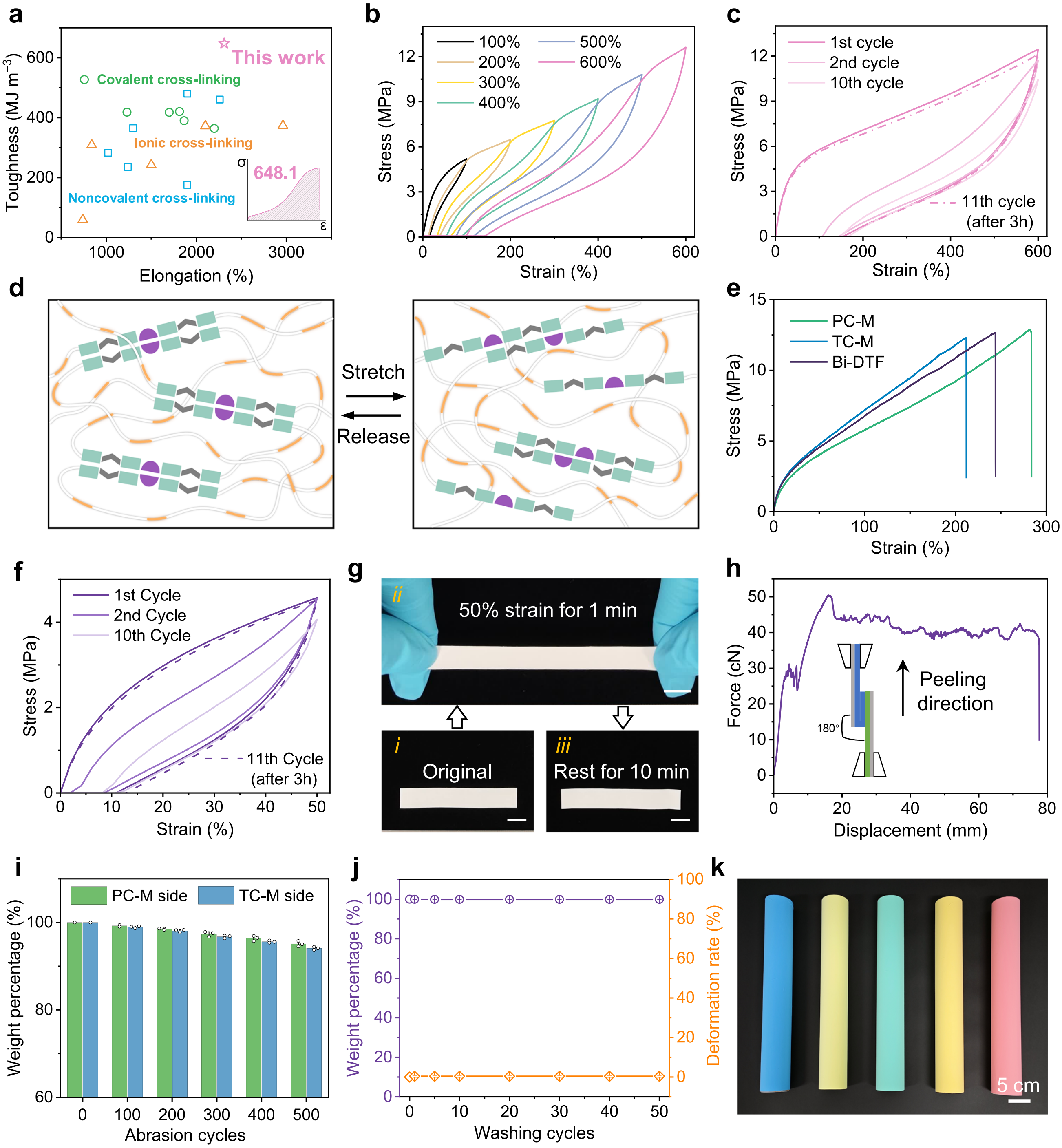

Fig. 3 | Mechanical and durability properties. a Comparison of the toughness and elongation of the PU elastomer in this work with those of cross-linked elastic membranes reported in the literature. The inset shows the typical stress-strain curve of the PU elastomer. **b** Cyclic loading-unloading tensile curves of the PU elastomer at increasing strain. **c** Tensile tests in successive loading-unloading cycles and after 3 h at 600 % strain. **d** Schematic illustration of the working mechanism of the PU during the stretch and release process. **e** Typical stress–strain curves of the PC-M, TC-M, and Bi-DTF. **f** Cyclic loading–unloading tensile curves of the Bi-DTF. **g** Photographs of the original, stretched, and recovered membranes. Scale bar: 1 cm. **h** The curves of peeling force as a function of displacement for composite sample. **i** Abrasion resistance and (**j**) washability of our textile. **k** Multicolor Bi-DTF collected on rollers. Scale bar: 5 cm. The error bars for **i** and **j** represent mean ± SD ($n = 3$ independent samples).

considered in the design of fibrous membranes. As seen in Supplementary Fig. 29, the water contact angle of PC-M was 139.3 ° due to the addition of PCN, while TC-M could spread and absorb liquid swiftly with the help of hydrophilic agents. Along with the interconnected channels between the fibers in an endeavor to achieve the necessary moisture permeability and directional water transport capacities[43].

To visualize the performance of the fabrics, commercial fabrics (Cotton, Coolmax, and Cool-fabric) were selected for comparison. We tested the water vapor transporting rate (WVTR) of fabrics at 15 and 35 °C, respectively (Fig. 4a). The results showed that the WVTR of fabrics at 15 °C was generally lower than that of fabrics stabilized at 35 °C attributed to the slower migration of water vapor at low temperatures, beneficial for the body insulation and moisturization. At

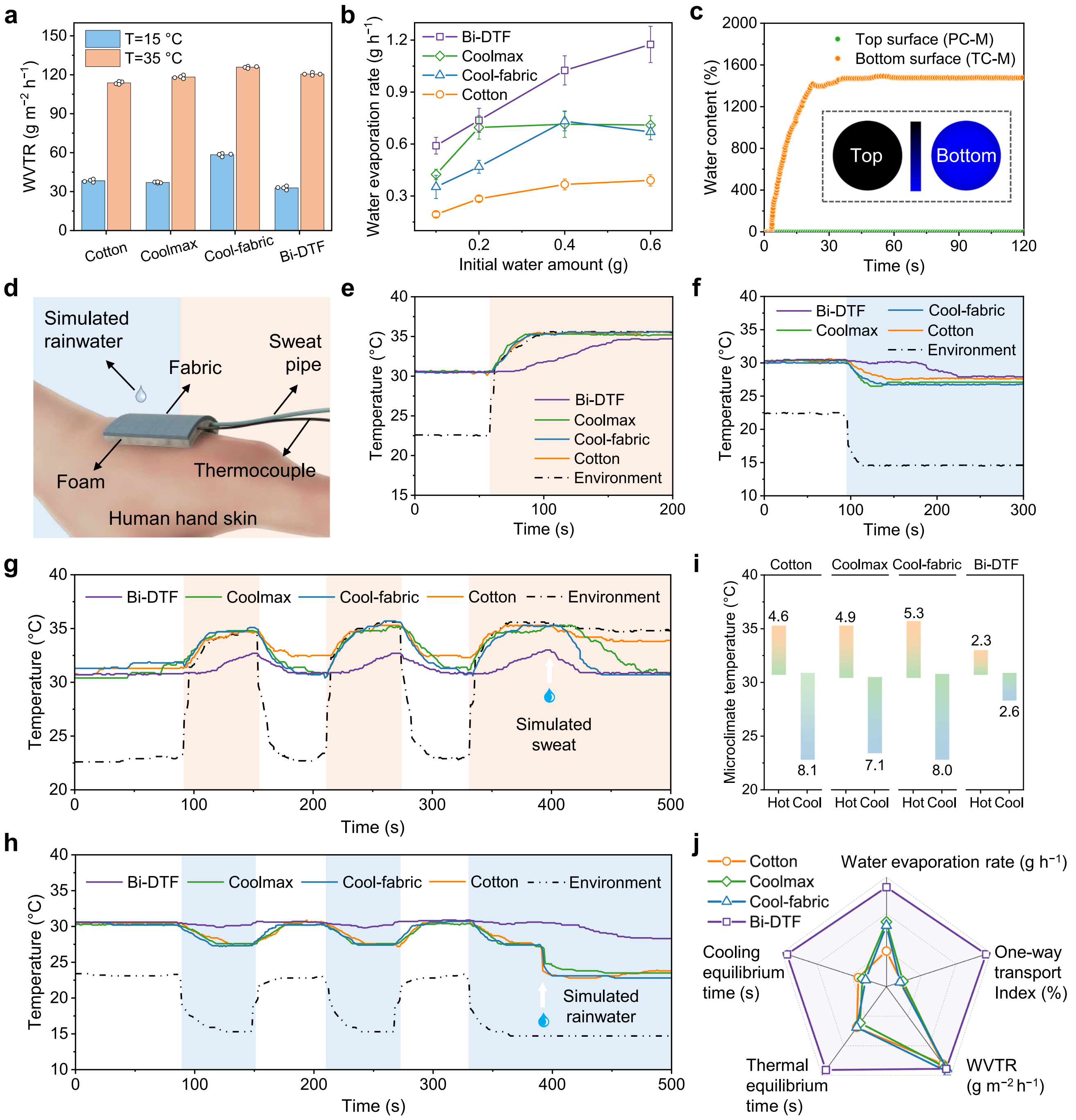

Fig. 4 | Dynamic moisture and thermal management performance. a WVTR of different fabrics at the temperature of 15 and 35 °C. **b** Water evaporation rate of fabrics at 35 °C. The relative water content on the top and bottom surfaces when the water was dropped on the (**c**) PC-M. **d** Schematic illustration of the thermoregulatory setup. **e** Cooling and (**f**) heating management properties of fabrics during high and low temperature environments. Cycling tests of fabrics from room temperature to (**g**) high temperature and (**h**) low temperature, respectively. **i** Maximum temperature difference of fabrics. **j** Comparison of self-adaptability of the Bi-DFT with related fabrics. The error bars for **a** and **b** represent mean ± SD (*n* = 4 independent samples).

35 °C, the moisture permeability of Bi-DTF was comparable to that of Coolmax, indicating that the porous structure of the fibrous membrane was sufficient to achieve the desired moisture permeability. We further compared the water evaporation rate of fabrics with varying initial water amounts under 35 °C (Fig. 4b). The values of other fabrics tended to be saturated when the initial water content reached 0.4 g, which is strongly related to the water diffusion behavior and adsorption/desorption rate (Supplementary Fig. 30)[44]. The Bi-DTF possessed a higher water evaporation rate than other fabrics, and it kept boosting with the increase of initial water amount. This enhanced water evaporation rate helps to speed up the sweat transmission rate in the body-textile microclimate and prolongs the cooling effect. We further investigated the relative water content changes about the two layers of the Bi-DTF by a moisture management tester. It showed a desired one-way water transport index (1338.6%) when water traveled from the PC-M to the TC-M and −1143.9% from the opposite direction (Fig. 4c and Supplementary Fig. 31). The differential wetting behavior between the two sides aids in the efficient management of sweat and prevents it from accumulating on the skin side, delivering uncomfortable adhesion; it also

inhibits the penetration of external rainwater, which may cause a chill sensation.

Previous researchers have mainly focused on the cooling and heating impacts of PCMs as monolayers during temperature variation, and given less consideration to the additive/detractive effect of moisture permeability on the overall wearable system[45]. The main factors determining the exchange process are human metabolic activity, the structural properties of the fabric, and the temperature/humidity of the macroenvironment[46]. By establishing the moisture/heat transfer models based on (phase change solid material) PC-S and Bi-DTF, the results can be concluded that the body-textile microclimate tends to be in the comfort zone through the coupling of the hydrophobic response layer/hydrophilic thermal conductivity layer (Supplement Fig. 32 and Note 2). On this basis, we proposed a setup to evaluate the dynamic comfort management performance of fabrics in adjusting the body-textile microenvironment when the circumstance switches, as illustrated in Fig. 4d. We first moved the palm from a comfortable (~22 °C) into a high temperature (~35 °C) environment. As the ambient temperature rose, the temperature of the microclimate covered by the other fabrics increased rapidly, whereas Bi-DTF experienced a gradually growing plateau due to heat absorption of the phase change components, with an equilibrium time of 94 s (Fig. 4e). When we shifted the palm from a comfortable to a low temperature (~15 °C) environment, the microclimate temperature of other fabrics also declined with the ambient. However, the Bi-DTF remained in the comfortable phase for a longer period before slowly decreasing with an equilibrium time of 124 s (Fig. 4f). The above results show that Bi-DTF has a better cooling and heating effect during environment switching.

We further tested the cyclic cooling and heating properties of the fabrics by shifting the palm three times and dripping water on the skin surface or external fabrics to simulate sweat/rainwater. As illustrated in Fig. 4g, during heating cycles, even though the Bi-DTF fluctuated slowly with ambient temperature, the microclimate of Bi-DTF exhibited a smaller temperature difference and managed perspiration more efficiently in the sweating condition. The Bi-DTF provided excellent thermal insulation and successfully blocked the intrusion of rainwater (Fig. 4h). On the contrary, the other fabrics switched rapidly with the ambient temperature after moving into the cold environment, and the microclimate temperature dropped rapidly, especially after dripping water, causing cold irritation to the skin and reducing the wearing comfort. Fig. 4i gives the threshold value of the body-textile microenvironment when covering different fabrics undergoing cyclic high and low-temperature environments, the Bi-DTF showed a maximum temperature difference of 2.3 and 2.6 °C, respectively. It is obvious that Bi-DTF can effectively absorb or release heat when dealing with high and low temperature switching to maintain the appropriate temperature range of the body-textile microenvironment, offering both physical and psychological comfort for individuals. We comprehensively compared the thermal and humidity comfort of various fabrics, and the results show that the fabrics are efficient in terms of self-adaptive performance (Fig. 4j).

Discussion

In this study, we have demonstrated the remarkable integration of toughness and self-adaptive Bi-DTF. This achievement originates from the optimized chain movements, characterized by reduced chain aggregation, improved compatibility with functional particles, and the construction of dynamic stress-dissipative networks. This hierarchical structural reconfiguration significantly raises the durability of composite fibrous membranes. The innovative employment of integrated heat adsorption/release and directional water transportation together effectively eliminates heat/cold irritation caused by environmental switching and ensures sufficient breathability, moisture permeability, and enhanced water evaporation rate. Compared with commercial textiles, Bi-DTF shows a maximum thermal temperature difference of only 2.3 °C and a cooling temperature difference of 2.6 °C when going through the heating and cooling cycles. Notably, there was no significant reduction in the energy storage capacity even after 100 recharging, 50 washing, or 500 rubbing cycles, indicating its high robustness. We believe the successful construction of attractive materials offers fascinating perspectives on the development of smart, toughness, and durable clothing that dynamically regulates comfort, prevents disease, and saves energy.

Methods

General

The experimental materials and detailed synthesis procedure of PCN are given in the Supplementary methods.

Preparation of PU

Typically, HDPOL (54 g, 0.03 mol) was vacuum heated at 110 °C and stirred for 2 h to remove the moisture in a flask. Subsequently, IPDI (23.3 g, 0.105 mol) was added, and DBTDL (0.1 g) was used as a catalyst, followed by stirring under nitrogen at 85 °C for 1 h. Then, BHO (12.3 g, 0,07 mol) as the chain extender was added to the system, and the temperature was raised to 180 °C under stirring for 30 min to obtain the final PU elastomer.

Fabrication of Fibrous Membranes

The precursor solutions for electrospinning were obtained by dissolving PU and nanofillers in the mixed solvent of DMF and EtOH (weight ratio of 1:1) at room temperature. For the preparation single-layer fibrous membranes with various loading, the weight ratio of PU, nanofillers, and mixed solvent were changed from 16:4:80, 16:11:73, 15:15:70, 14:21:65 to 12:28:60, respectively. Importantly, in order to enhance the hydrophilicity, a hydrophilic agent of TF (3 wt% relative to PU) was added to the prepared PU/BN/mixed solution. The resultant solutions were electrospun at a feeding rate of 3 mL h^{-1} under 30 kV in the high humidity environment (80 ± 5% RH). The Bi-DTF was fabricated layer-by-layer of the above-mentioned single-layer fibrous membranes with 60 wt% PCN loading and 50 wt% BN loading. The colorful appearance was obtained by additionally adding dye (1 wt% relative to PU) to the mixed PU/BN/TF solution.

Characterization

The ^{1}H-NMR spectra were recorded on a Bruker AVANCE III (400 MHz) spectrometer by using DMSO-d_6 as the solvent. GPC test was performed in THF solution at 35 °C with an elution rate of 1.0 mL min^{-1} on a Waters-E2695 GPC system equipped with a refractive index detector. The apparent molecular weights were determined on PLgel Mixed-B+ PLgel Mixed-C columns using linear poly(methyl methacrylate) standards. Fourier transform infrared spectroscopy (FTIR) was measured at room temperature on a Thermo Scientific Nicolet iS10 FT-IR spectrometer equipped with a diamond ATR crystal. 2D SAXS patterns were measured using a Bruker NANOSTAR instrument. The 1D WAXD curves were obtained from the DIFFRAC.SAXS software. The periodicity (L) was calculated by Bragg's Law:

$$L = \frac{2\pi}{q_{\max}} \tag{1}$$

where $q_{\max}$ is the value of the peak in the intensity curves.

The Glass Transition Temperature was acquired by Differential scanning calorimetry (DSC, DISCOVER 250). All the samples were heated from −90 °C to 150 °C at 20 °C min^{-1} and cooled at 20 °C min^{-1} from 150 °C to −90 °C. All data were collected during the second heating run from −90 °C to 150 °C at a scan rate of 10 °C min^{-1} to eliminate thermal history. The phase change behavior of samples was characterized by the DSC at a heating or cooling rate of 10 °C min^{-1} in a nitrogen atmosphere with a gas flow rate of 50 mL min^{-1}. The capacity of latent heat storage (ΔH_c and ΔH_m) was obtained from DSC. The DSC measurement uncertainties of enthalpy and temperature were 1.3% and 0.34 °C respectively.

The microstructures of samples were observed using FE-SEM (S-4800) and TEM (JEM-2100). The size distribution of PCN was determined by a nanoparticle size analyzer (ZEN3700). The porous architecture was evaluated utilizing a physisorption analyzer (ASAP 2460). The pore size distribution of the fibrous membranes was investigated by the capillary flow porometer (CFP-1100AI). The WCAs were obtained from a digital goniometer (SL200B). The reflectance of colorful fibrous samples in the visible wavelength range was measured using a UV-vis-NIR spectrophotometer (UV3600i Plus). The chromatic aberration DE*ab of textiles was tested by colorimeter (NR10QC). The Tensile tests and cyclic tensile deformation treatment were performed on an Instron 34 TM-5 universal machine. The stretching rate was set at 50 mm min^{-1}.

Measurement of through-plane and in-planed thermal conductivities

The specific heat capacity (C_p) was acquired by DSC using sapphire as the standard sample. The thermal diffusivity (α) was measured by adopting the laser flash method (LFA 467) at 25 °C. The through-plane and in-planed thermal conductivity (K) were calculated by the following equation:

$$K = \rho \cdot C_p \cdot \alpha \tag{2}$$

where ρ corresponds to the sample density.

WVTR measurement

The WVTR of fabrics was detected using an upright up method in accordance with ASTM E96 using a moisture tester (YG601H), with a modified temperature (15 ± 2 or 35 ± 2 °C) and humidity (50 ± 5% RH).

Water evaporation rate test

The deionized water was dropped on the inner side of the fabric, and then the fabric was hung in a controlled atmosphere (temperature of 35 ± 2 °C, humidity of 50 ± 5% RH, and air velocity of 0.3 ~ 0.5 m s^{-1}). The water evaporation rate is calculated as the weight change divided by the time required for mass balance.

Test of directional water transport behavior

The directional water transport behavior of the fabrics was quantitatively analyzed by MMT (SDL Atlas m290) according to AATCC 195-2009. The one-way water transfer index (R) was calculated by following equations in an in-built software:

$$R = \frac{\int(U_b) - \int(U_t)}{T} \tag{3}$$

where U_b is moisture content in the bottom layer, U_t is moisture content in the top layer and T is total testing time.

Peel test

The preparation of bi-layer membranes involves two steps: 1) Fabrication of the bottom layer by electrospinning on top of a glossy paper. 2) Fabrication of the top layer, half of the dried electrospun membrane (bottom layer) was covered with a glossy paper. The polymer was extruded and deposited onto the bottom layer to produce the second layer of electrospun membranes. To measure the adhesion strength between layers, the membrane was flipped up to 180 ° using an Instron at 50 mm min^{-1} crosshead speed.

Abrasion test

The abrasion test was conducted with a Martindale abrasion tester (YG401C) based on ISO 12947. The sample (38 mm) was mounted on the friction area and a loading weight of 260 g was applied, during which wool felt was used as the abrasive.

Washing resistance test

Following ISO 6330, the washability of the fabric was tested by adding standard detergent and washing the sample in an A-type standard washing machine (Y089D, Program No. 4H). The samples were 5 pieces of 10 × 10 cm and the total air-dry mass after addition of ballast was controlled with 2 kg. After the last rinse, the samples were dried by natural hanging.

Thermal management tests of fabrics

To verify the thermal management performance of the fabrics for actual wear, different fabrics were embedded into T-shirts and the temperature changes on the fabric surface were recorded with an infrared thermal camera. In addition, a test setup for body-textile microenvironment was built for practical application demonstration of environment switching. The temperature of the body-textile microenvironment was tracked using thermocouples. All the participants of the study gave written informed consent for the publication of the images and data. The authors affirm that human research participants provided written informed consent for publication of the images in Figs. 1 and 4.

Cohesive energy analysis

The MD simulation systems of PU are comprised of five polymer chains, each of which consists of two hard and two soft segments, in which the number of repeating units in the soft segments is 6 (Supplementary Figs. 33, 34). The molecular number ratios of PU/DMF and PU/DMF/EtOH simulation systems were set to 1/330 and 1/165/260, respectively, with a mass fraction of ~15 wt% for PU in the entire system and ~50 wt% for EtOH in the solvent (Supplementary Figs. 35, 36). The simulations were carried out using the Forcite module of the Materials Studio with COMPASS II force field.

The cohesive energy of a system of molecules, E_{coh}, is the average energy required to separate all molecules to an infinite distance from each other:

$$E_{coh} = -< E_{inter} > = < E_{intra} > - < E_{total} > \tag{4}$$

where E_{inter} is the total energy between all molecules, which is the total energy of a system (E_{total}), minus the intramolecular energy (E_{intra}). The bracket, “<…>”, represents an average over an NVT ensemble.

The cohesive energy density, *CED*, is simply the cohesive energy per unit of volume:

$$CED = \frac{E_{coh}}{V} \tag{5}$$

Statistics and reproducibility

Each experiment was repeated at least three times independently with similar results. All data are expressed as the mean ± standard deviation (SD).

Reporting summary

Further information on research design is available in the Nature Portfolio Reporting Summary linked to this article.

Data availability

All data are available from the corresponding author upon request. The data generated in this study are provided in the Source Data file. Source data are provided with this paper.

References

1. Wang, Z. et al. Self-sustaining personal all-day thermo regulatory clothing using only sunlight. *Science* **382**, 1291–1296 (2023).
2. Peng, Y. et al. Integrated cooling (i-Cool) textile of heat conduction and sweat transportation for personal perspiration management. *Nat. Commun.* **12**, 6122 (2021).
3. Peng, Y. et al. Integrated three-dimensional hydrophilicity/hydrophobicity design for artificial sweating skin (i-TRANS) mimicking human body perspiration. *Adv. Mater.* **34**, 2204168 (2022).
4. Fang, Y., Chen, G., Bick, M. & Chen, J. Smart textiles for personalized thermoregulation. *Chem. Soc. Rev.* **50**, 9357–9374 (2021).
5. Tansey, E. A. & Johnson, C. D. Recent advances in thermoregulation. *Adv. Physiol. Educ.* **39**, 139–148 (2015).
6. Dai, B. et al. Bioinspired Janus textile with conical micropores for human body moisture and thermal management. *Adv. Mater.* **31**, 1904113 (2019).
7. Lao, L., Shou, D., Wu, Y. & Fan, J. "Skin-like" fabric for personal moisture management. *Sci. Adv.* **6**, eaaz0013 (2020).
8. Zheng, S. et al. Hierarchical-morphology metafabric for scalable passive daytime radiative cooling. *Science* **373**, 692–696 (2021).
9. Wang, Y., Ma, K. & Xin, J. H. Stimuli-responsive bioinspired materials for controllable liquid manipulation: principles, fabrication, and applications. *Adv. Funct. Mater.* **28**, 1705128 (2018).
10. Liu, L., Zhang, Y., Zhang, S. & Tang, B. Advanced phase change materials from natural perspectives: structural design and functional applications. *Adv. Sci.* **10**, 2207652 (2023).
11. Chen, X. et al. Core-sheath heterogeneous interlocked conductive fiber enables smart textile for personalized healthcare and thermal management. *Small* **20**, 2308404 (2023).
12. Zhang, X. et al. Soft robotic textiles for adaptive personal thermal management. *Adv. Sci.* **11**, 2309605 (2024).
13. Wang, Y. et al. Reversible water transportation diode: temperature-adaptive smart janus textile for moisture/thermal management. *Adv. Funct. Mater.* **30**, 1907851 (2020).
14. Zhi, C. et al. Emerging trends of nanofibrous piezoelectric and triboelectric applications: mechanisms, electroactive materials, and designed architectures. *Adv. Mater.* **36**, 2401264 (2024).
15. Zuo, X., Fan, T., Qu, L., Zhang, X. & Miao, J. Smart multi-responsive aramid aerogel fiber enabled self-powered fabrics. *Nano Energy* **101**, 107559 (2022).
16. Wu, J. et al. A trimode thermoregulatory flexible fibrous membrane designed with hierarchical core-sheath fiber structure for wearable personal thermal management. *ACS Nano* **16**, 12801–12812 (2022).
17. Pielichowska, K. & Pielichowski, K. Phase change materials for thermal energy storage. *Prog. Mater. Sci.* **65**, 67–123 (2014).
18. Hu, X. et al. Novel personal cooling textiles revolutionizing human thermal management: principles, designs and applications. *Chem. Eng. J.* **499**, 155729 (2024).
19. Liu, H. et al. A thermoregulatory flexible phase change nonwoven for all-season high-efficiency wearable thermal management. *Nano-Micro Lett.* **15**, 2311–6706 (2023).
20. Gu, B. et al. A first method for increasing phase-change microcapsules in nanofiber textile through electrospinning. *Adv. Funct. Mater.* **35**, 2412089 (2025).
21. Li, X. et al. Wearable Janus-type film with integrated all-season active/passive thermal management, thermal camouflage, and ultra-high electromagnetic shielding efficiency tunable by origami process. *Adv. Funct. Mater.* **33**, 2212776 (2023).
22. Guo, Z. et al. Engineering of chain rigidity and hydrogen bond crosslinking toward ultra-strong, healable, recyclable, and water-resistant elastomers. *Adv. Mater.* **35**, 2300286 (2023).
23. Yao, Y. et al. A short review on self-healing thermoplastic polyurethanes. *Macromol. Chem. Phys.* **222**, 2100002 (2021).
24. He, W. et al. Establishing superfine nanofibrils for robust polyelectrolyte artificial spider silk and powerful artificial muscles. *Nat. Commun.* **15**, 3485 (2024).
25. Wong, C. & Choi, P. A free volume theory on the chain length dependence of the diffusivity of linear polymers. *Soft Matter* **15**, 9300–9309 (2019).
26. Bao, Q., Yang, Z. & Lu, Z. Molecular dynamics simulation of amorphous polyethylene (PE) under cyclic tensile-compressive loading below the glass transition temperature. *Polymer* **186**, 121968 (2020).
27. Guo, R. et al. Extremely strong and tough biodegradable poly(urethane) elastomers with unprecedented crack tolerance via hierarchical hydrogen-bonding interactions. *Adv. Mater.* **35**, 2212130 (2023).
28. Lai, Y. et al. Colorless, transparent, robust, and fast scratch-self-healing elastomers via a phase-locked dynamic bonds design. *Adv. Mater.* **30**, 1802556 (2018).
29. Liao, G. et al. Durability improvement of poroelastic road surface with treated rubber: Molecular dynamics simulation and experimental observations. *J. Clean. Prod.* **369**, 133334 (2022).
30. Huang, T. et al. Study on the compatibility between polyurethane and asphalt based on experiment and molecular dynamics simulation. *Case Stud. Constr. Mater.* **17**, e01424 (2022).
31. Song, P. & Wang, H. High-performance polymeric materials through hydrogen-bond cross-linking. *Adv. Mater.* **32**, 1901244 (2019).
32. Wu, J. et al. Facile fabrication of nanofiber- and micro/nanosphere-coordinated PVDF membrane with ultrahigh permeability of viscous water-in-oil emulsions. *J. Mater. Chem. A* **6**, 7014 (2018).
33. Jiang, S. et al. The structure of fibers produced by colloid-electrospinning depends on the aggregation state of particles in the electrospinning feed. *Polymer* **127**, 101–105 (2017).
34. Szewczyk, P. K. & Stachewicz, U. The impact of relative humidity on electrospun polymer fibers: From structural changes to fiber morphology. *Adv. Colloid Interface Sci.* **286**, 102315 (2020).
35. Gao, T. et al. Three-dimensional printed thermal regulation textiles. *ACS Nano* **11**, 11513–11520 (2017).
36. Miao, D. et al. A biomimetic transpiration textile for highly efficient personal drying and cooling. *Adv. Funct. Mater.* **31**, 2008705 (2021).
37. Aguirresarobe, R. H. et al. Healable and self-healing polyurethanes using dynamic chemistry. *Prog. Polym. Sci.* **114**, 101362 (2021).
38. Song, Y., Liu, Y., Qi, T. & Li, G. Towards dynamic but supertough healable polymers through biomimetic hierarchical hydrogen-bonding interactions. *Angew. Chem. -Int. Ed.* **57**, 13838–13842 (2018).
39. Affandi, N., Fadil, F. & Misnon, M. Preliminary Study on the Adhesion Strength of Electrospun Bi-Layer Membranes by 180 ° Peel Test. *Fiber Polym.* **20**, 1317–1322 (2019).
40. Al Harby, N. F., El-Batouti, M. & Elewa, M. M. Prospects of polymeric nanocomposite membranes for water purification and scalability and their health and environmental impacts: A review. *Nanomaterials* **12**, 3637 (2022).
41. Wang, G. et al. Phase change thermal storage materials for interdisciplinary applications. *Chem. Rev.* **123**, 6953–7024 (2023).
42. Shi, S. et al. A bionic skin for health management: excellent breathability, in situ sensing, and big data analysis. *Adv. Mater.* **36**, 2306435 (2023).
43. Lei, L. et al. Wettability gradient-induced diode: MXene-engineered membrane for passive-evaporative cooling. *Nano-Micro Lett.* **16**, 159 (2024).

44. Xiao, W. et al. A viscous-biofluid self-pumping organohydrogel dressing to accelerate diabetic wound healing. *Adv. Mater.* **36**, 2401539 (2024).
45. Jing, Y. et al. Ultraflexible, cost-effective and scalable polymer-based phase change composites via chemical cross-linking for wearable thermal management. *Nat. Commun.* **14**, 8060 (2023).
46. Chen, F., Fu, M., Li, Y., Shen, S. & Guo, X. Modelling and experimental study of thermo-physiological responses of human exercising in cold environments. *J. Therm. Biol.* **109**, 103316 (2022).

Acknowledgements

This work was supported by the the National Natural Science Foundation of China (No. 52473027, X.W.), the Textile Vision Basic Research Program (No. J202403, X.W.), and the AI-Enhanced Research Program of Shanghai Municipal Education Commission (No. SMEC-AI-DHUZ-06, X.W.).

Author contributions

Y.L. wrote the manuscript. C.Q., X.L., and C.D. organized the data. X.W and B.D. conceived and design the study. J.Y. supervised the project.

Competing interests

The authors declare no competing interests.

Additional information

Supplementary information The online version contains supplementary material available at https://doi.org/10.1038/s41467-025-62049-6.

Correspondence and requests for materials should be addressed to Xianfeng Wang or Bin Ding.

Peer review information *Nature Communications* thanks Fan Luo, and the other, anonymous, reviewer(s) for their contribution to the peer review of this work. A peer review file is available.

Reprints and permissions information is available at http://www.nature.com/reprints

Publisher's note Springer Nature remains neutral with regard to jurisdictional claims in published maps and institutional affiliations.

Open Access This article is licensed under a Creative Commons Attribution-NonCommercial-NoDerivatives 4.0 International License, which permits any non-commercial use, sharing, distribution and reproduction in any medium or format, as long as you give appropriate credit to the original author(s) and the source, provide a link to the Creative Commons licence, and indicate if you modified the licensed material. You do not have permission under this licence to share adapted material derived from this article or parts of it. The images or other third party material in this article are included in the article's Creative Commons licence, unless indicated otherwise in a credit line to the material. If material is not included in the article's Creative Commons licence and your intended use is not permitted by statutory regulation or exceeds the permitted use, you will need to obtain permission directly from the copyright holder. To view a copy of this licence, visit http://creativecommons.org/licenses/by-nc-nd/4.0/.

© The Author(s) 2025